SCATTERER DETECTION IN URBAN ENVIRONMENT USING PERSISTENT SCATTERER INTERFEROMETRY AND SAR TOMOGRAPHY

Alessandra Budillon[1], Michele Crosetto[2], Angel Caroline Jhonsy[1], Oriol Monserrat[2], Gilda Schirinzi[1]

[1]Dipartimento di Ingegneria, UniversitàdegliStudi di Napoli "Parthenope"
[2]Centre Tecnològic de Telecomunicacions de Catalunya (CTTC), Division of Geomatics

ABSTRACT

In the last decade, Persistent Scatterers Interferometry (PSI) and SAR tomography (TomoSAR) have been used for reconstructing the elevation profile of a scene, starting from a set of co-registered Synthetic Aperture Radar (SAR) images. The possible advantage of SAR tomography over classical interferometric methods, consists in the potential capability of improving the detection of single scatterers presenting stable proprieties over time (Persistent Scatterers or PS), as well as to enable the detection of multiple scatterers interfering within the same range-azimuth resolution cell. In urban environment, when only single dominant scatterers are present in each range-azimuth resolution cell, both methods can be exploited to estimate the altitude, deformation rate and thermal expansion of a subset of reliable scatterers, which are selected on the basis of different criteria.
This paper is focused on a performance analysis of the two class of methods, using the results obtained in urban environment on simulated and real TerraSAR-X data. A concise description of both techniques, along with a discussion on their potential capabilities in selecting the most reliable scatterers, is given.

Index Terms— SAR Interferometry, SAR Tomography, Permanent Scatterers, Differential Interferometry.

1. INTRODUCTION

The Earth monitoring capability of SAR sensors [1] has been increased substantially with the improvement in the spatial resolution along range and azimuth coordinates. With the evolution in the sensor's capabilities, the demand to boost the accuracy in the three dimensional (3D) localization of the scatterers and its density, without compromising the computational cost, is quite challenging. A renowned technique for Earth monitoring is Persistent Scatterer Interferometry [2, 3]. Being based on a phase-only model [4, 5], the method is well adopted in estimating the deformation velocity maps, thermal maps and residual topographic error (RTE). PSI techniques usually select the scatterers on the basis of coherence values in the stack of interferometric images. An extended model [6] qualifies the pixels on the basis of amplitude dispersion and separates the RTE, velocity and thermal contributions from the total observed deformation.
TomoSAR [7] is a multidimensional imaging technique that has proven its ability in localizing the scatterers, reconstructing the structures and analyzing the displacements and thermal contributions. SAR tomography, utilizes a stack of complex-valued images to discriminate the superimposed scatterers in the same range-azimuth cell, by synthesizing an elevation aperture to reconstruct a full 3D reflectivity profile along azimuth, range and elevation. The common problem faced in SAR tomography is the selection of the reliable scatterers and the outlier avoidance [8]. To this end, different Generalized Likelihood Ratio Tests [9, 10] have been introduced. These methods follow a Constant False Alarm Rate (CFAR) approach, by fixing the probability of false alarm to a given value, in such a way to mitigate the outlier occurrence.
With the advent of new generation of high resolution SAR sensors, for instance TerraSAR-X [11], with short wavelength of about ~3.1 cm, the sensitivity towards the deformation is further increased, which is a boon to PSI and TomoSAR techniques for a better reconstruction and estimation. In urban environment, when only single dominant scatterers are present in each range-azimuth resolution cell, both methods can be exploited to estimate the altitude, deformation rate and thermal expansion of a subset of reliable scatterers, which are selected on the basis of different criteria.
In this paper, the detection of single scatterers for reconstruction using the extended PSI model [6] and the TomoSAR Fast-Sup-GLRT [10] will be presented.

2. PERSISTENT SCATTERER INTERFEROMETRY

Let us consider a stack of M images collected with different orthogonal baselines s'_m, temporal baselines t_m and temperature baselines τ_m. We assume that within the same range–azimuth cell the scatterers at an elevation s_0 can undergo some motion and/or thermal dilation. We model the

motion as a temporally linear deformation $v_0 t_m$ with an average velocity v_0 and the thermal dilation as $k_0 \tau_m$, where k_0 represents the phase-to temperature sensitivity, which would tend to vary for each resolution cell (depending upon material and/or physical structure). PSI techniques [6] model the phase ϕ_m of the received signal at the m-th interferogram, in a generic image pixel as:

$$\phi_m = \frac{4\pi}{\lambda R_0} s_0 s'_m + \frac{4\pi}{\lambda} v_0 t_m + \frac{4\pi}{\lambda} k_0 \tau_m + w_m, \qquad (1)$$

Where λ is the operating wavelength, R_0 the distance between the image pixel and the reference antenna, and w_m the phase noise contribution. Only those pixels that have a good interferometric phase quality, usually in terms of the amplitude dispersion criterion [6], over the whole set of M-1 interferograms, are selected from this stack. The selected pixels are then connected by edges, computing the phase difference of each edge and getting a vector of differential interferometric wrapped phases. Given an edge, the unknown elevation, deformation and thermal dilation are estimated using a periodogram approach [12]. By integrating the unknowns over the whole set of edges that connects the PS, elevation map, deformation map and thermal map are obtained.

3. SAR TOMOGRAPHY

In contrast to classic PSI phase-only model, SAR tomography techniques [9] exploit both the amplitude and the phase information contained in the received signal $u(s'_m, t_m, \tau_m)$, that can be modeled as:

$$u(s'_m, t_m, \tau_m) = \int_{S_1}\int_{V_1}\int_{K_1} \tilde{\gamma}(s,v,k)\, e^{-j2\pi\left(\frac{2s'_m}{\lambda R_0}s + \frac{2t_m}{\lambda}v + \frac{2\tau_m}{\lambda}k\right)} ds\,dv\,dk \qquad (2)$$

where V_1 and K_1 are the range of values of v and k, and $\tilde{\gamma}(s,v,k) = \gamma(s)\delta(v - v_0)\delta(k - k_0)$. Then, the unknown elevation reflectivity profile $\gamma(s)$ can be derived from $\tilde{\gamma}(s,v,k)$ by sampling it in the values of v and k for which $\tilde{\gamma}$ assumes its maximum value.

The discrete version of the signal model (2) is obtained by discretizing s, v and k with steps $\Delta s = \rho_s/\eta_s$, $\Delta v = \rho_v/\eta_v$ and $\Delta k = \rho_\kappa/\eta_\kappa$, where η_s, η_v and η_k are oversampling factors (necessarily greater than or equal to one) and ρ_s, ρ_v and ρ_k are the Rayleigh resolutions given by:

$$\rho_S = \frac{\lambda R_0}{2S_B}; \quad \rho_v = \frac{\lambda}{2t_B}; \quad \rho_k = \frac{\lambda}{2T_B}; \qquad (3)$$

With S_B, t_B and T_B the overall baseline, time and temperature spans of the measured data, respectively.
The discretized model is:

$$\mathbf{u} = \mathbf{\Phi\gamma} + \mathbf{w}, \qquad (4)$$

where $\mathbf{w}$ is an $M\times1$ vector representing noise and clutter, and $\mathbf{\Phi}$ is an $M\times N$ measurement matrix, whose m-th row $\boldsymbol{\phi}_m$ is given by $vec(\mathbf{\Phi}_{m3})$, where vec is the operator transforming a three-dimensional matrix of size $N_s\times N_v\times N_k$ in a row vector of size $N=N_sN_vN_k$. by loading in the vector all the elements of the matrix scanned in a preassigned order, and $\mathbf{\Phi}_{m3}$ is the three-dimensional matrix of size $N_s\times N_v\times N_k$, whose element of entries (i,l,n) is given by:

$$\{\mathbf{\Phi}_{m3}\}_{i\,l\,n} = \frac{1}{\sqrt{N}} e^{j\left(\frac{4\pi}{\lambda R_0}s_i s'_m + \frac{4\pi}{\lambda}v_l t_m + \frac{4\pi}{\lambda}k_n \tau_m\right)}. \qquad (5)$$

In order to detect a single scatterer and to estimate its unknown elevation, deformation and thermal dilation, a GLRT (Generalized Likelihood Ratio Test) approach can be used. The detection problem in [9] is formulated in terms of K_{max}+1 statistical hypothesis. We restrict our assumption to the presence of only single scatterers (K_{max}=1) in the same range-azimuth resolution cell. Then, we have the following statistical hypothesis

H_0: absence of scatterers,
H_1: presence of a single scatterer.

The Fast-Sup-GLRT Detector [10], based on GLRT [13], when $K_{\max}$=1, applies the following binary test:

$$\Lambda_1'(\mathbf{u}) = \frac{\left[\mathbf{u}^H\mathbf{u}\right]}{\left[\mathbf{u}^H\left(\mathbf{I} - \mathbf{\Phi}_{\hat{\Omega}_1}\left(\mathbf{\Phi}_{\hat{\Omega}_1}^H\mathbf{\Phi}_{\hat{\Omega}_1}\right)^{-1}\mathbf{\Phi}_{\hat{\Omega}_1}^H\right)\mathbf{u}\right]} \underset{H_1}{\overset{H_{i0}}{<>}} T_1', \qquad (6)$$

where $\mathbf{I}$ is the $M\times M$ identity matrix, $\mathbf{\Phi}_{\hat{\Omega}_1}$ is a column vector of size $M\times1$ obtained by extracting a column from $\mathbf{\Phi}$ and H denotes the Hermitian. The threshold T_1' can be derived by using Mote Carlo simulation and following a CFAR approach, consisting in setting T_1' in such a way to obtain an assigned probability of false alarm $P_{FA} = P(H_1|H_0)$.
A summary of the two approaches, PSI and Fast-Sup-GLRT, is shown in table I.

3. EXPERIMENTAL RESULTS

A comparison of the two approaches will be conducted on simulated and real TerraSAR-X data (see Table 2 for system parameters). We consider 28 TerraSAR-X images whose spatial and temporal baselines and temperatures are reported in Fig. 1, where the distribution of the spatial baselines (orthogonal component) vs. the temporal baselines (a), and of the temperature values vs. the temporal baselines (b) are shown. The average air temperature for each image is used. The total spatial baselines span is about 507 m, thus the Rayleigh resolution in elevation is 19 m, the total temporal span is 1.89 years, and the temperature values range is 19 ^{o}C. In Fig. 1 it can be seen that the two conditions specified in [6, 14], that the observed period has to be as large as possible, and that it is important to minimize the correlation between spatial baselines (orthogonal component), temporal baselines and temperature values, are satisfied. The slant range resolution is 1.2 m, the resolution in azimuth is 3.3 m. In case of the Fast-Sup-GLRT the thresholds have been computed by Monte Carlo simulation for the considered system parameters (Table 2), fixing $P_{FA}=10^{-3}$, the oversampling factor is $\eta_s=6$, thus the achieved resolution in elevation is 6.3 m. The two detector are tested on the urban area of Barcelona, Spain, where the Arts Hotel Tower, a 44-storey, 154-m tall, is located. The tower is surrounded by an external perimeter structure completely in steel, so we expect a high sensitivity to temperature changes. In Fig. 2 the SAR intensity images of test site is presented. In Fig. 3 the scatterers detected by the PSI approach and the Fast-Sup-GLRT, on a 3D Google Earth optical image, are respectively shown in (a) and (b). In Fig. 4 we present the average deformation velocity map, estimated by the PSI approach and the Fast-Sup-GLRT, respectively shown in (a) and (b). In Fig. 5 we present the thermal map, estimated by the PSI approach and the Fast-Sup-GLRT, respectively shown in (a) and (b).

A detailed analysis will be given in the final version of the paper. The total number of single scatterers detected with the two approaches will be specified, and on set of scatterers jointly detected by the two algorithms the expectation and the standard deviation of the differences among the estimates along the elevation, velocity and thermal dilation will be evaluated. The comparison will be done also on the computation time.

Table 1. Synthetic description of the techniques.

Technique	**Pixel Selection Criterion**	**Resolution**	**Outlier Rejection**
Extended PSI Model	Amplitude dispersion	Optimum interval selection	PSI quality Index
Fast-Sup-GLRT	CFAR based Threshold	Super-resolution	Based on Probability of False Alarm

Table 2. TerraSAR-X parameters.

TerraSAR-X parameters	
Wavelength	0.031 m
View angle	35°
Range distance	618 km

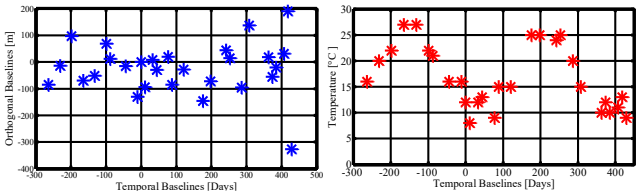

(a) (b)

Figure 1: (a) Distribution of the spatial baselines (orthogonal component) vs. the temporal baselines; (b) distribution of the temperature values vs. the temporal baselines.

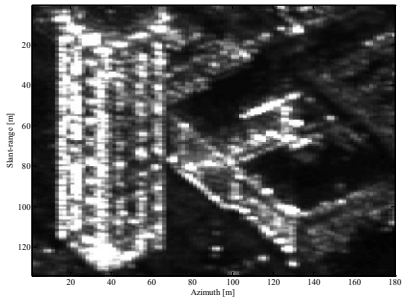

Figure 2: Intensity SAR image of Arts Hotel Tower, Barcelona, Spain (Copyright DLR 2007-2010).

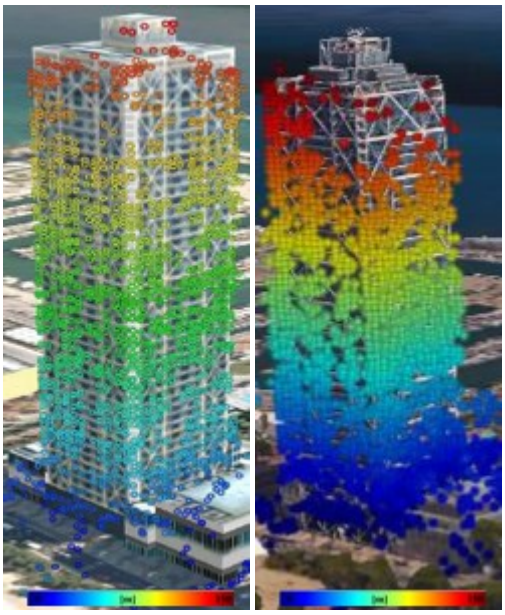

(a) (b)

Figure 3: Detected Single Scatterers with color code representing the height in meters. (a) Scatterers detected by Extend PSI model; (b) Scatterers detected by Fast-Sup-GLRT.

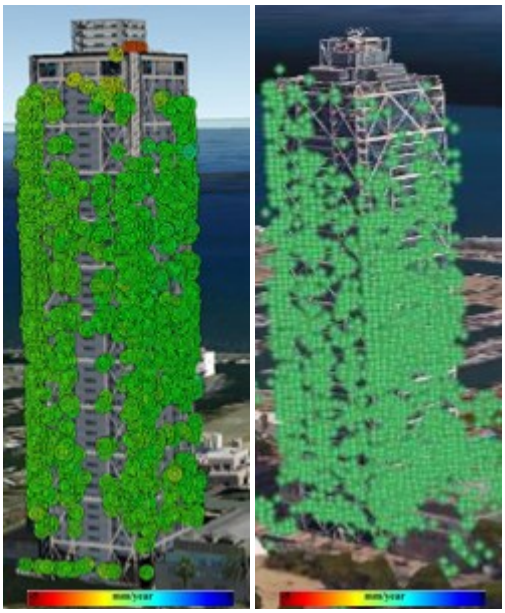

(a) (b)

Figure 4: Estimated average deformation velocity map, with velocity expressed in mm/year by (a) Extended PSI model; (b) Fast-Sup-GLRT.

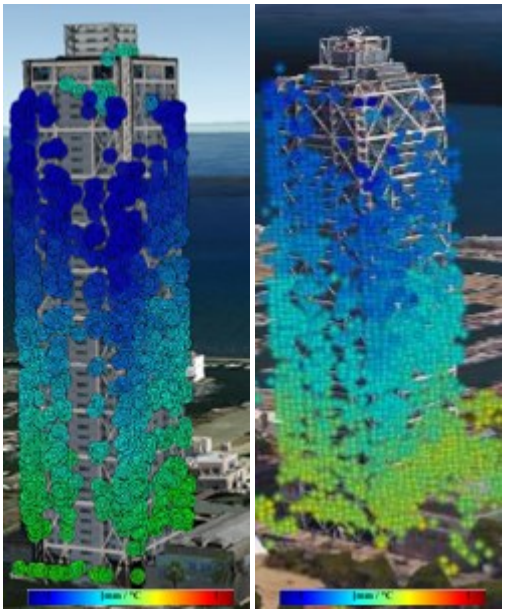

(a) (b)

Figure 5: Estimated thermal dilation map, with dilation coefficient expressed in mm/°C by (a) Extended PSI model; (b) Fast-Sup-GLRT.

6. REFERENCES

[1] G. Fornaro, V. Pascazio, "SAR Interferometry and Tomography: Theory and Applications", Academic Press Library in Signal Processing, Communications and Radar Signal Processing, Vol. 2, Cap. 20, pp. 1043-1117, Elsevier Ltd. 2013.

[2] A. Ferretti, C. Prati, and F. Rocca, "Permanent scatterers in SAR interferometry," IEEE Trans. Geosci. Remote Sens., Vol. 39 (1), pp. 8–20, Jan. 2001.

[3] M. Crosetto, O. Monserrat, M. Cuevas-González, N. Devanthéry, B. Crippa, "Persistent Scatterer Interferometry: a review," ISPRS Journal of Photogrammetry and Remote Sensing, 115, 78-89, 2016.

[4] O. Monserrat, M. Crosetto, R. Iglesias, B. Crippa, "Persistent scatterer interferometry: Potential, limits and initial C- and X-band comparison", Photogrammetric Engineering and Remote Sensing, Vol. 76, pp. 1061-1069, 2010

[5] M. Crosetto, O. Monserrat, M. Cuevas, N. Devanthéry, "Persistent Scatterer Interferometry:a review" ISPRS J. Photogramm. Remote Sens.,Vol.115,pp.78-89,2015

[6] O. Monserrat, M. Crosetto, M. Cuevas, B. Crippa, "The Thermal Expansion Component of Persistent Scatterer Interferometry Observations", IEEE Geosci. Remote Sens. Letters, Vol. 8, pp. 864 - 868, 2011.

[7] F. Baselice, A. Budillon, G. Ferraioli, V. Pascazio, G. Schirinzi, "Multibaseline SAR Interferometry from Complex Data", IEEE J. of Selected Topics in Applied Earth Obs. and Remote Sens., Vol. 7 (7), pp. 2911-2918, 2014

[8] A. Budillon, G. Ferraioli, G. Schirinzi. "Localization Performance of Multiple Scatterers in Compressive Sampling SAR Tomography: Results on COSMO-SkyMed Data", IEEE J. of Selected Topics in Applied Earth Obs. and Remote Sens., Vol. 7 (7), pp. 2902-2910, 2014.

[9] A. Budillon, G. Schirinzi, "GLRT Based on Support Estimation for Multiple Scatterers Detection in SAR Tomography", IEEE J. of Selected Topics in Applied Earth Obs. and Remote Sens., Vol. 9 (3), pp. 1086 – 1094, 2016.

[10] A. Budillon, A. Johnsy, G. Schirinzi, "A modified statistical test based on support estimation for multiple scatterers detection in SAR tomography",IEEE International Geoscience and Remote Sensing Symposium (IGARSS),2016

[11] M. Eineder, N. Adam, R. Bamler, N. Yague-Martinez, and H. Breit, "Spaceborne spotlight SAR interferometry with TerraSAR-X," IEEE Trans. Geosci. Remote Sens., vol. 47, no. 5, pp. 1524–1535, 2009.

[12] E. Biescas, M. Crosetto, M. Agudo, O. Monserrat, and B. Crippa, "Two radar interferometric approaches to monitor slow and fast land deformations," J. Survey. Eng., vol. 133, no. 2, pp. 66–71, May 2007.

[13] A. Budillon, G. Schirinzi, "Performance evaluation of a GLRT moving target detector for TerraSAR-X along-track interferometric data", IEEE Trans. Geosci. Remote Sens.,Vol. 53 (6) pp. 3350-3360, 2015.

[14] D. Reale, G. Fornaro, A. Pauciullo, "Extension of 4-D SAR Imaging to the Monitoring of Thermally Dilating Scatterers", IEEE Trans. Geosci. Rem. Senss., Vol. 51, pp. 5296 - 5306, 2013.